3D-printed vascular networks direct therapeutic angiogenesis in ischaemia

T. Mirabella[1,2], J. W. MacArthur[3], D. Cheng[1,2], C. K. Ozaki[4], Y. J. Woo[5], M. T. Yang[6] and C. S. Chen[1,2]*

Arterial bypass grafts remain the gold standard for the treatment of end-stage ischaemic disease. Yet patients unable to tolerate the cardiovascular stress of arterial surgery or those with unreconstructable disease would benefit from grafts that are able to induce therapeutic angiogenesis. Here, we introduce an approach whereby implantation of 3D-printed grafts containing endothelial-cell-lined lumens induces spontaneous, geometrically guided generation of collateral circulation in ischaemic settings. In rodent models of hind limb ischaemia and myocardial infarction, we demonstrate that the vascular patches rescue perfusion of distal tissues, preventing capillary loss, muscle atrophy and loss of function. Inhibiting anastomoses between the construct and the host's local capillary beds, or implanting constructs with unpatterned endothelial cells, abrogates reperfusion. Our 3D-printed grafts constitute an efficient and scalable approach to engineer vascular patches that are able to guide rapid therapeutic angiogenesis and perfusion for the treatment of ischaemic diseases.

schaemic cardiovascular disease remains the leading cause of morbidity and mortality in the United States and continues to grow at an alarming rate worldwide[1,2]. Impaired blood circulation to different organs and tissues underlies debilitating conditions such as limb ischaemia, heart failure and stroke[3–5]. Although percutaneous revascularization and artery bypass surgery continue to be mainstay treatments for alleviating ischaemia in large vessel occlusive artery disease, the generation of collateral circulation via the recruitment of small vessels, or therapeutic angiogenesis, could offer an additional (even adjunctive) approach that would address an unmet need. Traditional open surgical bypass is not well tolerated in many ischaemic patients, due to comorbidities that drive periprocedural complications[6–11], and anatomic and durability barriers continue to limit more widespread application of endovascular therapies. Furthermore, in many instances, disease is not limited to large arteries and additional approaches are needed to enhance perfusion at the microvasculature level[12–14].

Initial efforts to develop pro-angiogenic therapies focused on the delivery of angiogenic growth factors (for example, vascular endothelial growth factor (VEGF) and fibroblast growth factor) to an ischaemic site[15–17]. However, it was quickly realized that such soluble factors are rapidly extracted and eliminated from a site. Moreover, the disappointing results of pro-angiogenic VEGF therapy were linked to a significant increase in oedema[18]. Subsequent attempts used controlled-release biomaterials or expression vectors delivered to either local cells or injected engineered cells[15,19–22]. Cytokine- and cell-based micro-revascularization showed remarkable initial experimental promise, but then clinically insignificant benefits in prospective randomized clinical trials[23]. Recent studies in rodents have shown that injection of vascular endothelial cells and stromal cells attract host vessels to invade into a site and form new vessels. However, the invasion process takes weeks and the resultant vasculature is randomly organized, unlike in native capillary networks[24,25]. Thus, no current therapies to restore microcirculation have reached mainstream clinical practice.
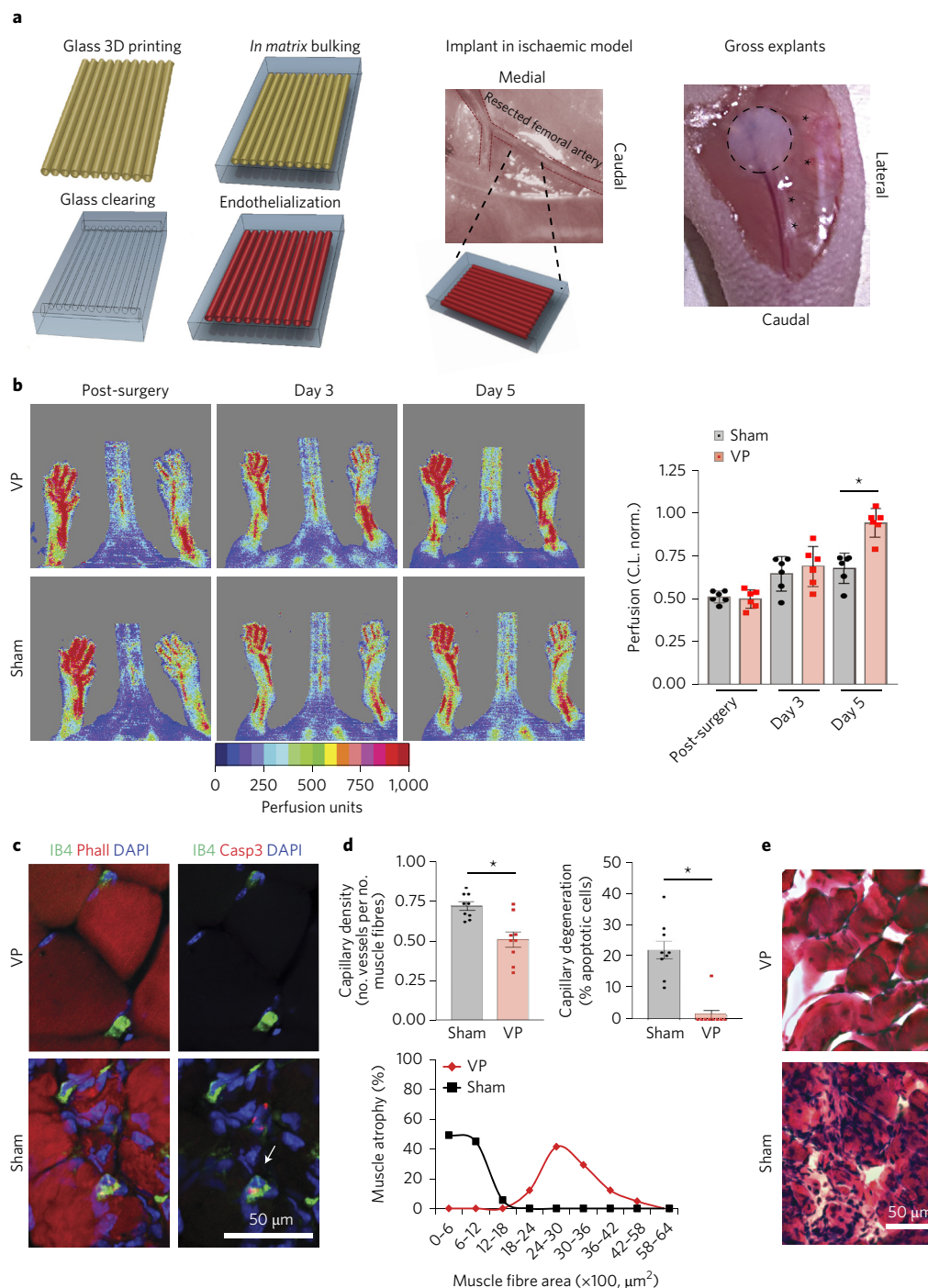
Within the tissue engineering field, recent studies have demonstrated that pre-organizing endothelial cells into defined network architectures within small tissue-engineered constructs can significantly enhance the speed and extent of vascularization of the construct on implantation[26–28]. However, the extent to which such an approach could be scaled and adapted to treat ischaemia of endogenous mammalian tissues remains unclear.

Here, we present an approach using 3D printing to pre-organize endothelial cells into patterned channels within a fibrin patch, which on implantation, facilitated rapid invasion and integration of small collaterals from the host to generate perfused, functional blood vessels that mirrored the architecture of the implanted grafts. By using constructs containing long, centimetre-scale channels orientated in parallel as a means to direct revascularization from well-perfused sites into surrounding ischaemic tissues, we demonstrate the potential utility of the approach in two relevant models of ischaemic disease.

Results

3D-printed vascular patches functionally engraft in vivo and rescue perfusion and function of ischaemic tissues. In this study, we set out to test whether organizing endothelial cells into patterned channels within an implantable, fully degradable fibrin patch would enhance perfusion in rodent models of ischaemia. To engineer endothelial networks, we used a recently described method to 3D print sugar filaments into a network, encapsulate the network in a fibrin gel, dissolve the sugar to leave behind channels and inject endothelial cells to fill the channels (Fig. 1a)[29]. To assess the efficacy and translational value of these patterned constructs in vivo, we implanted them in a mouse model of hind limb ischaemia and tracked perfusion of distal limbs from 5 to 21 days. In this model, occlusion of the left femoral artery distal to the inferior epigastric and profunda femoris arteries (injury site) caused a 50% postoperative decrease in perfusion of the distal ischaemic limb, as measured by laser Doppler imaging (Fig. 1b). In mice implanted at the injury

Figure 1 | Fabricated VPs rescue perfusion in hind limb ischaemia. a, Left: schematic of VP fabrication; carbohydrate glasses are 3D printed as parallel filaments. After PDLGA-coating and fibrin (10 mg ml⁻¹) bulking, the sacrificial sugar is removed by overnight washing in PBS. The remaining channels are endothelialized by flowing HUVECs and shear-conditioning the confluent monolayer overnight, before implantation in ischaemic hind limb mice. Middle: representation of the patches implantation site within the cauterized femoral artery space. Right: representation of the patches retrieved 5 days after implantation (stars mark collateral arteries and veins). **b**, Left: laser Doppler imaging of distal limbs over time (post-surgery, day 3 and day 5) in the two groups (VP and sham). Right: histogram of perfusion levels of the ischaemic limb. Perfusion units of the ischaemic limb were normalized to the perfusion units of the contralateral (non-ischaemic) limb (C.L. norm.) and are expressed as the fold change. Data are expressed as mean ± s.d.; $N = 6$ animals per group; *$P < 0.01$, t-test. **c**, Staining of gastrocnemius muscle sections (25 μm thick) with phalloidin (cytoarchitecture; Phall; red), IB4 (capillaries; IB4; green) and activated caspase 3 (apoptosis; DAPI; blue). Shown are representative images (Spin Disk Confocal, 20 μm stack) for the two groups (VP and sham). Arrow points at apoptotic endothelial cell. **d**, Capillary density, capillary degeneration (% apoptotic endothelial cells in capillaries) and muscle atrophy (distribution of muscle fibre area expressed as the frequency percentage for each area subgroup, within 0–6,000 μm²) in the gastrocnemius muscle of the two groups (VP and sham). Total number of capillaries analysed were 55 and 211, respectively, for the VP and sham groups. Data are expressed as mean ± s.e.m.; $N = 3$ animals per group, three gastrocnemius muscle sections per mouse; *$P < 0.02$, Mann–Whitney U-test. **e**, H&E staining of 15 μm sections of gastrocnemius muscles in the two groups (VP and sham), revealing hypercellularization and fibrosis initiation in the mice without implants.
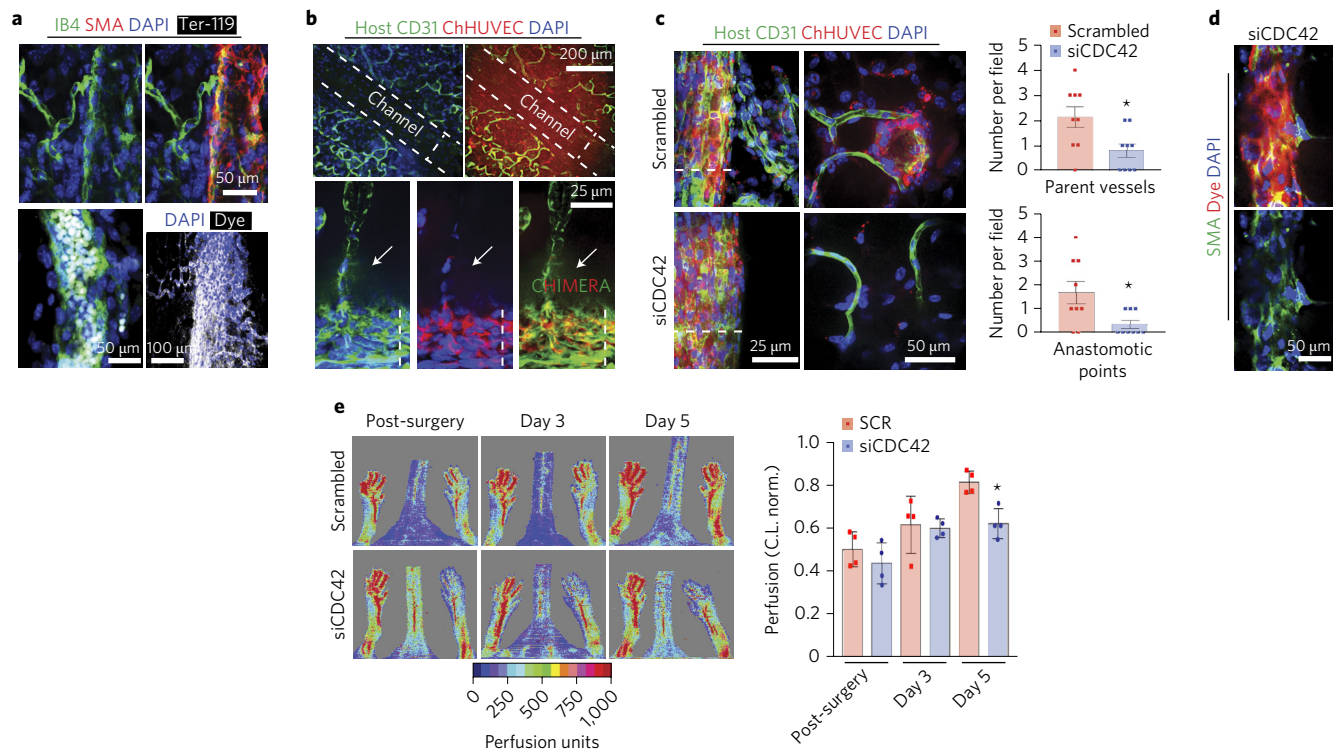
Figure 2 | Host-driven biointegration of grafts drives perfusion of ischaemic limb. a, VPs explanted at day 5 stained for isolectin B4 (IB4; green), showing both host capillary and VP endothelium, mouse specific smooth muscle actin-alpha (SMA; red), showing host-derived smooth muscle cells and Ter-119 (black), showing the red blood cells. The lower right panel shows a channel perfused by host vasculature, as demonstrated by dye localization immediately following systemic perfusion of dye-labelled dextran. Nuclei are labelled by DAPI. **b,c**, Explanted VPs at day 5 are stained for host vessels (mouse CD31; green); endogenous red fluorescence of implanted mCherry HUVECs is also shown. In **b**, upper panels show low-magnification images of a channel (dashed lines) within the VP implant and lower panels show high-magnification images of the channel, which is chimeric (wall covered by both host CD31 and implanted mCherry HUVECs) and anastomosed to a host capillary (arrows). **c**, *Ex vivo* VPs (scrambled and silenced for CDC42). Left panels show the patterned channels (dashed lines) as mosaic multicellular composites (endogenous fluorescence for implanted mCherry HUVECs and mouse CD31-stained host endothelial cells); right panels show anastomosis between host capillaries and parental VP-derived vessels (ChHUVECs); histograms show the number of VP-derived vessels (parent vessels) and the number of anastomotic points between parent and host vessels (quantified in nine fields from VPs explanted from three mice per group; scrambled versus siCDC42). Data are expressed as mean ± s.e.m.; *$P < 0.04$; Mann–Whitney U-test. **d**, CDC42-silenced VPs explanted at day 5 stained with mouse specific SMA, showing host-derived smooth muscle cells and UAE-1 lectin, as a systemically injected dye (red), showing human endothelial cells of the implanted channels, to demonstrate vascular integrity and function. Panels **a–d** are representative 100 μm stack images. **e**, Left: laser Doppler imaging of distal limbs over time (post-surgery, day 3 and day 5) in the two groups: control VPs (scrambled) and VPs where CDC42 has been knocked down (siCDC42). Right: histogram shows perfusion levels of the ischaemic limb. Perfusion units of the ischaemic limb were normalized to perfusion units of the contralateral (non-ischaemic) limb (C.L. norm.) and are expressed as the fold change. Data are expressed as mean ± s.d.; $N = 4$ animals per group; *$P < 0.05$; t-test.

site with vascular patches (VPs), perfusion measured distally at the feet progressively increased over time, to reach the value of the contralateral, non-ischaemic limb by 5 days postoperatively (Fig. 1b). In the sham group, perfusion did not substantially improve from the postoperative levels.

Ischaemia experienced in the limb distal to the site of artery occlusion induced, as expected, an angiogenic response in the gastrocnemius muscle of the lower limb, as indicated by the number of vessels normalized to the number of muscle fibres (Fig. 1c). The number of capillaries normalized to the number of muscle fibres, was abnormally high in the sham group compared with the VP group (Fig. 1d). On closer examination of histologic sections, we also observed a substantial increase in apoptotic endothelial cells within capillaries of the sham group, but not in the VP group. In VP-implanted mice, muscle fibres appeared healthy, with a characteristic distribution of diameters (Fig. 1d). In contrast, in the sham group there was degeneration of muscle tissue. Fibres were smaller (area $< 1,800\,\mu m^2$) and showed a diffuse hypercellularity indicative of early fibrosis (Fig. 1e). Thus, the implanted VPs appeared to restore perfusion to distal tissues and rescue ischaemic muscle damage.

Direct anastomoses of VPs with host vasculature drives functional perfusion. To better understand how the VPs restored distal perfusion, we examined the vasculature at the site of implantation. Laser Doppler imaging revealed progressively improved perfusion both up- and downstream of the VPs by day 3, suggestive of the establishment of collateral circulation through the construct (Supplementary Fig. 1). On retrieval at day 5, approximately two-thirds of the endothelialized channels originally implanted were visibly present in constructs, with the attrition probably because of partial resorption of the fibrin patch. Histology of the explanted construct confirmed the presence of host capillary vessels directly connecting to the pre-patterned endothelial channels, with new smooth muscle actin-positive mural cells lining the patterned vessels and blood perfused within them (Fig. 2a). To further confirm perfusion of channels via direct anastomosis to the systemic circulation, dye-labelled dextran was perfused systemically by tail vein injection minutes before tissue explantation. The presence of dye within the channels confirmed perfusion by the host vasculature (Fig. 2a). About 90% of the retrieved channels were functional (dextran perfused). Labelling with monoclonal anti-mouse

CD31 antibody revealed that these capillaries were of host origin at the interface between the implant and the surrounding tissue (Fig. 2b). Long and branched capillaries transited across the implant and reached the patterned construct, lining the edges of the channels. The vascular walls of the patterned vasculature were chimerically occupied by both implanted endothelial cells and host endothelial cells, and coupled to host capillaries. EphrinB2 and EphB4 staining further confirmed that most endothelial cells within the microchannels expressed the vein marker EphB4 and only a small subset of endothelial cells expressed ephrinB2, consistent with the nature of the implanted human umbilical endothelial cells (HUVECs) and host capillary endothelial cell invasion (Supplementary Fig. 2).

Although connectivity between host and implant vasculature could be critical to the therapeutic effect of the constructs, another possibility is that the implanted endothelial cells simply provide paracrine support for host vasculature. To test this, we implanted constructs containing endothelial cells in which the expression of the sprout-inducing guanosine triphosphate hydrolase enzyme, cell division control protein 42 (CDC42), was silenced by short interfering RNA (siRNA). SiRNA treated cells (siCDC42) were confirmed to lack expression of CDC42, with reduced invasive sprouting *in vitro*, but retained normal viability (Supplementary Fig. 3). *In vivo*, siCDC42 versus control VPs revealed substantially reduced integration between host capillaries and patterned engineered vasculature (Fig. 2c), with fewer vessels arising from the implanted VPs (parent vessels) and lower anastomotic connections between parent and host vessels. Channels where CDC42 was silenced still recruited host mural cells, but with decreased coverage (Fig. 2d). Anastomosis between channels and host capillaries were fewer in number, with systemically injected lectin still found within the channel walls (Fig. 2d). However, at a functional level, laser Doppler imaging showed a significant decrease of distal perfusion to ischaemic limbs in mice implanted with siCDC42 VPs, compared with scrambled control VPs (Fig. 2e). Thus, biointegration of vascular graft and functional recovery result from local connection between host and implant vasculature, giving rise to a functionally significant collateral circulation.

Patterning of vascular architecture is critical to therapeutic benefit. To clarify whether the therapeutic effect of the implant was merely due to the presence of the exogenous endothelial cells secreting angiocrine cues or because the endothelial cells were patterned in a certain architecture, we compared constructs containing endothelialized channels in VPs (as before) with: (1) constructs carrying the same number of endothelial cells randomly embedded into fibrin and not patterned with channels (endothelial patches; EP) and; (2) fibrin patterned with channels but not seeded with cells (acellular patches; AP). Mice implanted with APs or EPs were not able to rescue perfusion of the ischaemic limb and were comparable to non-treated shams, even in 21-day long-term studies (Fig. 3 and Supplementary Fig. 4). Moreover, the histology of the EPs confirmed a lack of substantial invasion or anastomosis of host vessels with implant vessels, compared with the patterned constructs (Supplementary Fig. 5). These results suggest that the presence of only endothelial cells, without concomitant organization into vessel-like structures, fails to establish the organized collateral circulation needed to perfuse distal ischaemic sites.

We next examined whether changes in the geometry of the vascular channels, rather than their presence or absence, could impact their therapeutic function. Decreasing the diameter of the 3D-printed channels from 400 μm (VPs) to 200 μm (Sm_D VPs), while keeping the amount of HUVECs seeded constant (for example, by increasing the number of channels per patch), decreased the ability of the patch to rescue perfusion of distal limbs to the extent that the effect was no longer significantly different from the
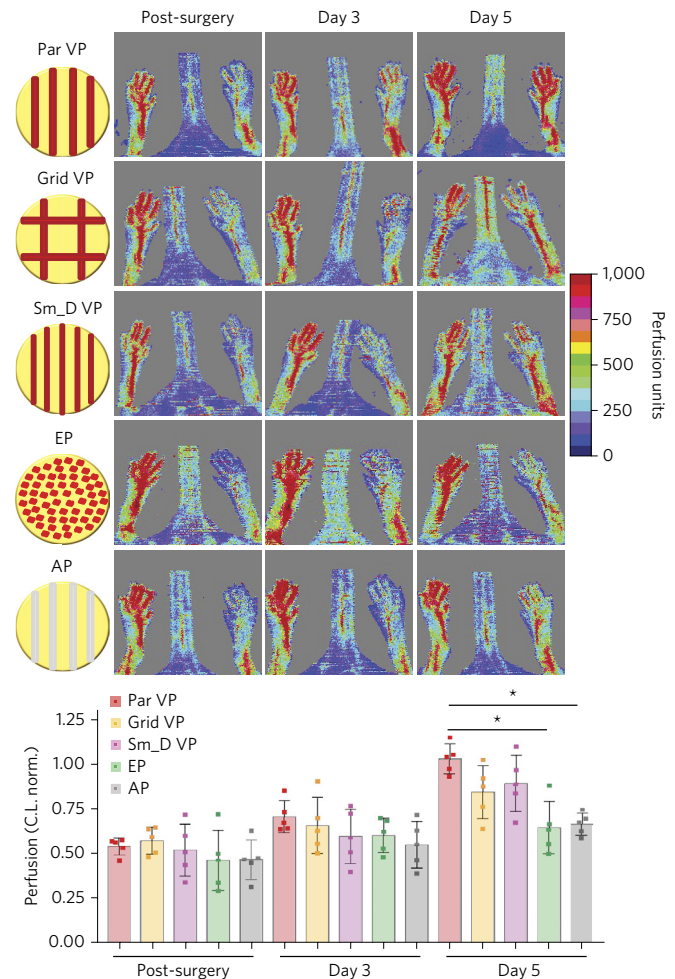
Figure 3 | Geometric patterning within VPs impacts perfusion performance. Upper: laser Doppler imaging of distal limbs over time (post-surgery, day 3 and day 5) in the five groups: Par VP = VPs where channels were orientated parallel to each other; Grid VP = VPs where channels were orientated orthogonally to each other to form a grid; Sm_D VP = VPs with parallel channels of smaller diameter; EP = endothelial patches where HUVECs were randomly embedded into the fibrin matrix; and AP = acellular patches containing patterned, not endothelialized channels. Lower: histograms of perfusion levels of the ischaemic limb. Perfusion units of the ischaemic limb were normalized to perfusion units of the contralateral (non-ischaemic) limb (C.L. norm.) and are expressed as the fold change. Data are expressed as mean ± s.d.; $N = 5$ animals per group; *$P < 0.01$; ANOVA with Bonferroni correction.

negative control groups (EPs and APs). We also generated constructs where microchannels were arranged in a grid shape (Grid VPs) compared with our standard constructs where microchannels ran parallel to each other (Par VPs), keeping the number of channels present in each patch constant. Grid VP implants exhibited reduced efficacy in rescuing perfusion compared with Par VPs, to the extent that they were not significantly different from the negative control groups. Together, these results suggest that the geometric design of the vascular channels within the patch impacts its ability to rescue perfusion, perhaps by affecting the efficiency of directing blood volume and flow from non-ischaemic to ischaemic regions, a parameter critical for recovery of distal perfusion and function.

3D-printed VPs rescue cardiac function in a model of myocardial infarction. Given the potential utility of VPs to rescue perfusion in
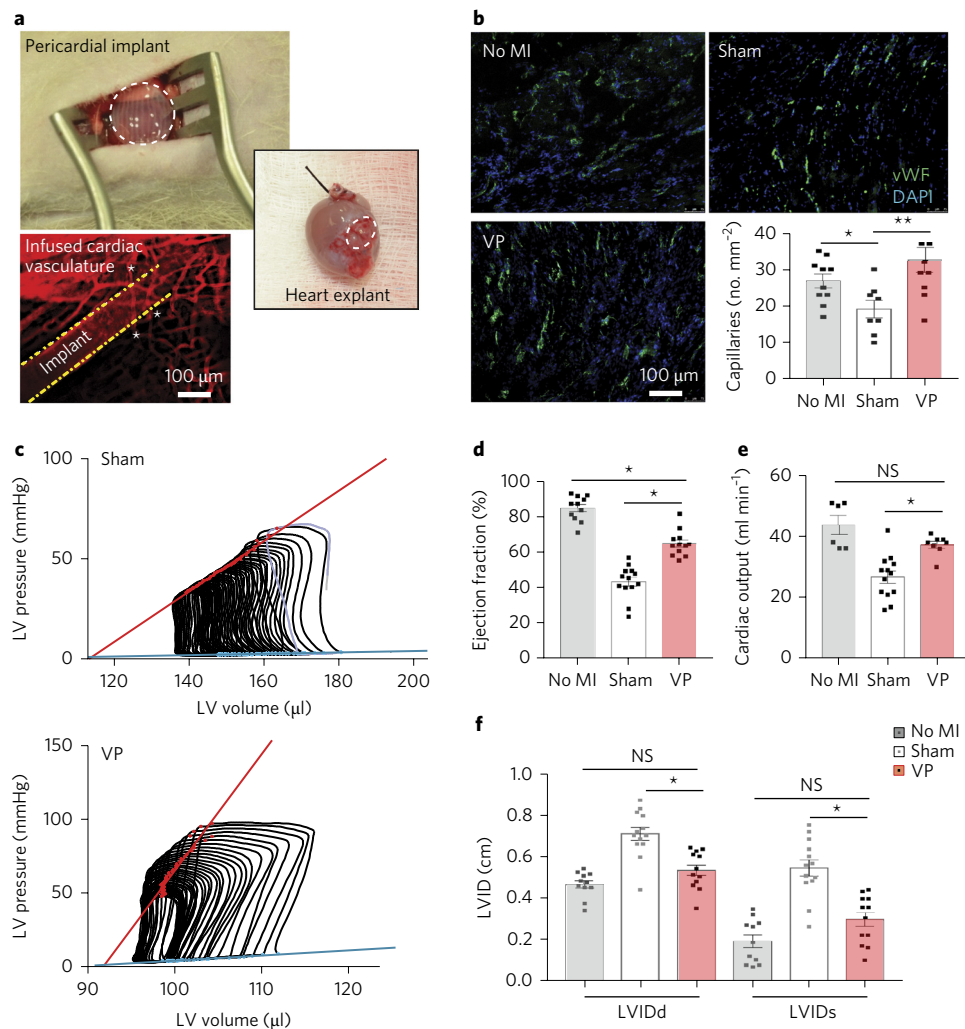
Figure 4 | Fabricated VPs rescue cardiac function after MI in rats. a, Upper: angled view of a rat undergoing implantation of VPs (dashed circle), placed on the left ventricle (LV) of the infarcted heart. Middle: an explanted heart shows the vascularized region where the implant was placed 4 weeks prior (inset, dashed circle). Lower: the DiI-infused vasculature within the explanted patch is shown in red, with channel borders marked with dashed lines and point of connections between the channel and capillaries marked by stars. **b**, Immunofluorescence images of explanted heart sections (15 μm thick) stained for vWF (green). Histogram shows the vascular density for the no MI, sham and VP groups, quantified as the number of vWF-positive capillaries per mm^2 of cardiac tissue. Heart capillaries were quantified in three fields per heart. Data are expressed as mean ± s.e.m.; sham group $N = 8$ explanted hearts; no MI and VP groups, $N = 10$ explanted hearts each; *$P < 0.03$, **$P < 0.01$; Mann–Whitney U-test. **c**, Representative pressure–volume loops for infarcted hearts that received either no treatment (sham) or VPs. **d**, Ejection fraction of infarcted hearts in the no MI, sham and VP groups. **e**, Cardiac output of infarcted hearts in the no MI, sham and VP groups. **f**, LVIDd and LVIDs in the no MI, sham and VP groups. In **d–f**, data are expressed as mean ± s.e.m.; no MI group $N = 11$ rats; sham and VP groups, $N = 13$ rats each; *$P < 0.01$; NS, not significant; ANOVA with Bonferroni correction.

the ischaemic limb, we sought to investigate whether the approach could improve outcomes in the more demanding setting of cardiac infarction, where perfusion deficits lead to irreversible damage. A well-defined myocardial infarction (MI) was generated by ligation of the left anterior descending coronary artery in athymic rats[30–34]. Constructs patterned with aligned channels of endothelial cells (VPs) were placed on the surface of the heart spanning over the border between non-ischaemic and ischaemic zones of the underlying heart (Fig. 4a). Healthy rats (no MI) and MI rats that received saline injections following artery ligation (sham) were used as treatment controls. At 4 weeks after the surgery, both non-invasive functional measurements and terminal histology assessments were performed in the ischaemic region of the rat hearts. Gross analysis of the explanted rat hearts revealed increased vascularization throughout the implant and surrounding native tissue. The vasculature within the explanted patch consisted of dense networks of host capillaries connecting with long segments of parent channels, which were

functionally integrated as they were DiI perfused after systemic infusion (Fig. 4a). Immunohistochemical staining of von Willebrand factor (vWF)-positive vessels in the ischaemic zone of the cardiac tissue indicated loss of capillaries in untreated infarcted hearts compared with healthy controls, and a substantial increase in capillary densities following treatment with VPs (Fig. 4b). Aortic flow probe and intraventricular pressure–volume conductance measurements were obtained to determine cardiac output and other functional parameters (Fig. 4c–e); analysis indicated that hearts from the sham group exhibited half the ejection fraction and cardiac output of the no MI controls (Fig. 4d,e). In contrast, VPs resulted in partial rescue of cardiac function, with an ejection fraction and a cardiac output close to that measured in the healthy controls (Fig. 4d,e). Moreover, using transthoracic echocardiographic analysis, the left ventricular internal dimension (LVID) could be non-invasively measured for hearts in diastole (LVIDd) and systole (LVIDs) (Fig. 4f). Untreated ischaemic hearts exhibited substantial increases in LVIDd and

LVIDs compared with healthy controls, while rats treated with VPs did not develop significant ventricle dilation (Fig. 4f). Together, these results demonstrate substantial rescue of cardiac function following a major ischaemic injury.

Discussion

Previous work has demonstrated that one can induce robust elaboration of capillary beds simply by injecting a variety of pro-angiogenic growth factors, gene therapy vectors, cells and/or biomaterials[15–22]. Here, by implanting a patch containing pre-engineered vessels, we not only observed enhanced angiogenesis, but the engineered vessels also became integrated with the host vasculature and resulted in significant perfusion of distal ischaemic tissues. The demonstration that the therapeutic effect required anastomosis between host and engineered vasculature suggests that the larger calibre (150–400 μm diameter) engineered vessels may significantly enhance the volume of blood delivered distally. Indeed, to deliver blood across centimetre distances only via the highly branched, cascading structure of capillary beds is biomechanically highly inefficient[35,36]. It is thus not entirely surprising that we observed that constructs containing disorganized endothelial cells—previously shown to give rise to highly branched capillary beds[25]—fail to rescue sufficient circulation to meet the demands of a major artery. The fact that capillaries may not be well suited to address ischaemia, except in cases where low capillary density is the primary limitation to tissue perfusion, could contribute to the lack of success of therapeutic angiogenesis in clinical ischaemia, despite promise in small rodent studies. Nevertheless, further studies in larger animal models demanding rescue of perfusion across larger scale ischaemic territories will be required to evaluate whether the strategy of implanting orientated patterns of engineered vessels would ultimately have therapeutic merit at the clinical scale.

Additive manufacturing, or 3D printing, has rapidly advanced as an approach to fabricate numerous types of complex structures across research and industry sectors[37]. 3D printing has been adopted to fabricate various types of engineered tissue structures, primarily through the use of low-pressure nozzles to print natural or synthetic hydrogels in the presence or absence of suspended cells[38]. We and others have recently extended these efforts by using 3D printing to generate microvessel networks in vitro that allow one to model or grow thicker tissues that require perfusion[29,39]. Here, we used 3D printing to generate patterns of vasculature in vitro and were able to provide a path for engineering host vasculature in vivo. Given that vascular architecture follows specific patterns conserved across many species[35,36], but is also distinct in different tissue settings, it is not surprising that our studies demonstrate that the geometry of the channels is a design parameter that impacts functionality of the implant; we anticipate that the pattern of engineered vasculature used in constructs could dramatically impact its performance in promoting circulation in different contexts. Thus, this vascular guidance technology could provide a means to not only re-wire circulatory pathways for a variety of applications, but that each application may need to be customized with different architectural and functional outcomes depending on the host vascular context.

Given the loss of rescue in acellular implants and those containing CDC42-deficient cells, the in vivo dynamic vascular remodelling activity of the constructs appears to require functional endothelial cells. Beyond remodelling activity, a polarized endothelium prevents direct contact of materials with blood, which otherwise leads to rapid vessel occlusion[14,40,41]. The current proof-of-concept study used a construct containing human endothelial cells implanted in immunocompromised rodents, an approach that takes into consideration the post-surgery medications that bypass candidate patients undergo. Although innate immunity is intact in these models, a fully immunocompetent host might be expected to modulate the response to the implant. Immune cells contribute to angiogenesis,

vascular remodelling and inflammation[42], each of which could either improve or mute the therapeutic benefits of the approach. Thus, a study using autologous cells in an immunocompetent host, or heterologous cells in larger immunosuppressed animals, is warranted to further evaluate the possible clinical outcomes of this approach. Moreover, because of the multifactorial nature of ischaemic cardiovascular diseases, the choice of animal model (small versus large; obese/diabetic and ageing versus no risk factors) and endpoint are considerations that could impact outcomes; in part, the lack of significant clinical successes in this arena to date speak to the uncertain nature of the extent to which preclinical models predict outcomes of revascularization therapies in humans[43–47]. Even with these clinical development challenges met, it should be recognized that a cell-based therapy ultimately remains a resource intensive endeavour that is only considered given that acellular alternatives may not be as effective of the RhoGTPase inhibitors Y27632 (10 μM), ML141 (30 μM) and NSC23766 (50 μM).

Although treatment of focal blockages in large arteries has largely been addressed through a combination of percutaneous interventions and surgical bypass grafts[6–14], approaches to enhance development of collateral circulation at the level of small vessels, as demonstrated here, could provide additional therapeutic benefit. Such approaches may not only help the many patients that also experience small vessel disease, but also could be used to induce additional collaterals in at-risk patients as prophylaxis against progression of organ malperfusion. In addition, for inoperable patients (due to anatomic factors or medical comorbidities[6–10]), induction of collateral circulation could be an alternative to relieve ischaemia.

Methods

Cell culture and Matrigel assay. Primary HUVECs (Lonza) were cultured for up to seven passages on 0.1% (wt/vol) gelatin-coated dishes in endothelial cell growth medium (EGM-2; Lonza), maintained at 37 °C in 100% humidified air containing 5% carbon dioxide, with the medium changed every other day. Certificate of analysis for source, identity and infective agents screening was provided by the vendor, and mycoplasma testing was routinely run as good practice. HUVECs labelled with the fluorophore mCherry (gifted by R. Tsien) were used for ex vivo imaging purposes.

To assess in vitro vascular network formation, HUVECs were plated onto a thin layer (50 μl cm^{-2}) of Matrigel (Basement Membrane Matrix; BD Biosciences) at a density of 10,000 cells cm^{-2} and cultured in EGM-2 medium for 16 h in the presence of the RhoGTPase inhibitors Y27632 (10 μM), ML141 (30 μM) and NSC23766 (50 μM) (Sigma).

CDC42 knock-down. For silencing CDC42, 60% confluent HUVECs were transfected for 6 h with 20 nM CDC42 siRNA (Hs_CDC42_7 FlexiTube siRNA; Qiagen) or scrambled in a solution of Lipofectamine RNAiMAX (Invitrogen), according to the manufacturer's instructions. Expression levels of CDC42 were assessed by real time polymerase chain reaction (PCR; qScript cDNA SuperMix, Quanta Bioscience, for cDNA synthesis; QuantiTect SYBR Green PCR Kit, Qiagen, for PCR reaction) and by antibody staining (mouse anti-CDC42, Clone 44; BD Biosciences). The glyceraldehyde 3-phosphate dehydrogenase (GAPDH) primers used were: forward 5′-GTCTCCTCTGACTTCAACAGCG-3′ and reverse 3′-ACCACCCTGTTGCTGTAGCCAA-5′; human CDC42 primers used were: forward 5′-TGACAGATTACGACCGCTGAGTT-3′ and reverse 3′-GGAGTCTTTGGACAGTGGTGAG-5′. Channels within moulds were seeded with transfected HUVECs and either left in culture for the apoptosis and sprouting assay or implanted in vivo in a model of hind limb ischaemia. Active caspase 3 (Rb pAb, Abcam) staining was used to determine the percentage of apoptotic cells within channels. The growth of angiogenic sprouts from patterned vessels was tested after a 4 day culture in fibroblast conditioned media/EGM-2 medium (1:1), followed by fixation in 4% paraformaldehyde (Sigma) for 30 min and phalloidin (Invitrogen) staining for 1 h.

3D printing of carbohydrate glass patterns. A mixture of 100 g isomalt, 10 g dextran (86 kDa) and 60 ml reverse osmosis water (≥18 MΩ; Millipore) was warmed to 155 °C to remove most of the water and form a liquid glass. The hot mixture was poured into a 50 ml syringe that was maintained at 110 °C. The syringe was mounted on a ShopBot Desktop, custom-modified 3D printer to use for additive layer manufacturing with an added RAMBo 1.3 (Ultimachine) circuit board. Carbohydrate glass lattices were printed at 110 °C under nitrogen pressure with pneumatic control through an 18-gauge (0.84 mm internal diameter) steel nozzle, vitrified to 50 °C and then air-sprayed (Badger Air-Brush Model

175-7) with a 5 mg ml⁻¹ solution of poly-D-lactic-glycolic acid (PDLGA; Purac) in chloroform. Glass moulds were either immediately encapsulated in extracellular matrix or stored at 90 °F until use to protect hygroscopic properties.

Casting of vascular structures. A fibrin gel solution (10 mg ml⁻¹) was generated by mixing fibrinogen, thrombin (2.5 U ml⁻¹ final concentration) and phosphate-buffered saline (PBS), and then dispensed to encapsulate the printed carbohydrate glass moulds. Fibrin gels were allowed to polymerize for 15 min at 37 °C, placed in PBS, then washed until the carbohydrate glass was completely dissolved. The encapsulated patterns were ported at each corner using a 2 mm biopsy punch and the dissolved sugar solution was flushed out with PBS. A suspension of 3.5×10^6 cells ml⁻¹ HUVECs in medium was injected into the ports of the hollow mould architecture and allowed to attach to channel lumens in static culture for 1 h before being placed on a platform rocker in a humidified 37 °C incubator, to induce gravity-driven flow overnight. In some cases, HUVECs were co-injected with 1 mg ml⁻¹ type I collagen into the moulds with similar bioactivity following implantation. For experiments with randomly patterned HUVECs, cells were mixed into a bulk fibrin gel as it polymerized and then similarly placed on a platform rocker in a humidified 37 °C incubator overnight before implantation.

Mouse ischaemic hind limb model. Female nude mice (7- to 10-week-old; Taconic) were anaesthetized with 1–3% isoflurane at flow rate of 1 litre min⁻¹ and body temperature was maintained on a circulating heated water pad, during both the surgical procedure and laser Doppler imaging monitoring. Following skin incision, the femoral neurovascular pedicle was visualized under a stereoscope and the left femoral nerve and vein were carefully separated from the femoral artery. The femoral artery abscission was executed below the deep branch by electrocauterization. In this moderate model of hind limb ischaemia, the perfusion of the operated distal limb was assessed immediately post-surgery to be half of the contralateral. This model did not develop spontaneous limb necrosis or self-amputation for the duration of the study, mirroring symptoms of significant ischaemia, such as the ankle–brachial index (ABI) and histopathological features, in patients with peripheral artery disease. Once the artery was occluded, implants were positioned with channels in parallel to the downward running femoral artery and the surgical site was sutured; the site was inspected for infection and scarring for the duration of the study. Mice of the sham group underwent electrocauterization of the femoral artery to generate ischaemia; no implant was inserted and the site was sutured. Laser Doppler imaging (Moor Instrument) was performed as described previously[48–50], at 16 h and on day 3 and day 5 after surgery. Mice were scanned at a standardized working distance of 32 cm. Blood flow through the feet and the supine inferior limbs was documented as a two-dimensional (2D) colour-coded image (scan modus settings: 4–10 ms pixel⁻¹, resolution 256×256 pixels). Results are expressed as fold increase/decrease of perfusion units, with respect to the contralateral foot (=1). The LaMorte power calculation was adopted to estimate the sample size to detect a specific effect. All data points collected were included in the analysis. Animals were randomly assigned to groups. All outcomes were assessed disregarding of group allocation. All animal procedures were performed at the Charles River campus animal Facility, Boston University, under a protocol approved by the Institutional Animal Care and Use Committee. All experiments pertaining to this investigation conformed to the "Guide for the Care and Use of Laboratory Animals"[51].

Rat MI model. Athymic male rnu rats weighing 170–190 g were obtained from Charles River Laboratories. The continuous delivery of 3% isoflurane was used to anaesthetize the rats. A 16-gauge angiocatheter was used for endotracheal intubation and connected to mechanical ventilation (Hallowell EMC); 1% isoflurane was maintained throughout the operation. A thoracotomy was performed through the left 4th intercostal space, the heart was exposed, and a 7-0 polypropylene suture was placed around the left anterior descending artery 2 mm below the left atrium. The suture was briefly snared to verify the size and location of myocardial ischaemia, based on colour change, and permanently tied down to produce a large anterolateral MI. The animals were then randomized to three different groups: healthy rats (no MI), untreated operated rats injected with saline (sham) and rats implanted with patterned constructs (affixed with 7-0 polypropylene suture to the centre of the infarct). The thoracotomy was closed in multiple layers and tissue adhesive (VetBond; 3M) was applied over the incision, followed by recovery from anaesthesia. Buprenorphine (0.5 mg kg⁻¹) was administered for postoperative pain control. The LaMorte power calculation was adopted to estimate the sample size to detect a specific effect. All data points collected were included in the analysis. Animals were randomly assigned to groups. All outcomes were assessed disregarding of group allocation. All experiments pertaining to this investigation conformed to ref. [51]. The protocol was approved by the Institutional Animal Use and Care Committee of the University of Pennsylvania.

Echocardiographic and haemodynamic assessment. Left ventricular geometry and function were evaluated pre-operatively and at 4 weeks in all animals. A Phillips Sonos 5500 revD ultrasound system (Philips Medical Systems) was used, with a 12 MHz transducer at an image depth of 2 cm. Left ventricular parasternal short axis 2D and M-mode images at the papillary muscle level were used to obtain echocardiographic data.

Four weeks after left anterior descending artery ligation, all three groups of animals underwent invasive haemodynamic measurements with a pressure–volume conductance catheter (SPR-869; Millar Instruments). The catheter was calibrated via 5-point-cuvette linear interpolation with parallel conductance subtraction by the hypertonic saline method. Rats were anaesthetized as above and the catheter was introduced into the left ventricle utilizing a closed-chest approach via the right carotid artery. Measurements were obtained before and during inferior vena cava occlusion to produce static and dynamic pressure–volume loops under varying load conditions. Data were recorded and analysed with LabChart software (version 7; AD instruments). Finally, cardiac output was assessed by placing a 2.5 mm peri-aortic Doppler flow probe (Transonic Systems) around the ascending aorta.

Visualization and functional assessment of perfusion in the implanted vasculature. Five days following implantation, mice were anaesthetized with 3% isoflurane continuously delivered and then intravenously injected with 200 µl of ulex europaeus agglutinin I (UEA-I) lectin solution (Rhodamine or fluorescein isothiocyanate (FITC)-conjugated; Vectors Lab) or 500 µl of 1 mg mL⁻¹ dextran (70 KDa; FITC or Texas Red conjugated; Molecular probes). Mice were kept under anaesthesia (1% isoflurane) for 15 min and then euthanized by cervical dislocation. Implants were harvested in 4% paraformaldehyde and either whole-mount imaged or submerged in OCT (TissueTek), frozen and stored at −80 °C until imaging. Four weeks after implantation, a subset of rats were anaesthetized with 3% isoflurane continuously delivered, endotracheally intubated with a 16-gauge angiocatheter connected to mechanical ventilation (Hallowell EMC). A median sternotomy was performed, exposing the heart and ascending aorta. The ascending aorta was clamped and then a 16-gauge needle was inserted into the proximal ascending aorta and connected to pressure tubing with a three way stopcock at its end. An atriotomy was made in the right atrium with scissors and PBS was infused through the aortic needle until effluent from the right atrium was clear. Next, 10 cc of DiI solution (D-282, Invitrogen) was infused through the aortic needle. Hearts were explanted, submerged in OCT, frozen and stored at −80 °C. Assessment for blood vessels was conducted on cryosections of 100–200 µm thickness.

Postmortem tissue preparation, staining and imaging. Animals were euthanized according to protocols approved by the Institutional Animal Use and Care Committee. Tissues and implanted constructs were dissected, OCT-embedded and snap frozen in liquid nitrogen. Histology sections (15 to 100 µm thickness), whole mount preparation, and haematoxylin and eosin (H&E) staining were performed by standard procedures. A solution of 5% goat serum and 0.1% Triton X-100 in PBS ×1 was used for the 2 h, room-temperature blocking before staining. Primary antibodies were incubated at 4 °C overnight, including rat anti-mouse Ter-119 (1:100; BD Pharmingen), monoclonal rat anti-mouse PECAM-1 (1:100; BD Pharmingen), sheep anti-vWF (conjugated to FITC, 1:100; Abcam), goat polyclonal anti-EphB4 (N-19, 1:100; Santa Cruz) and rabbit polyclonal Ephrin B2 (1:100; Novus Biologicals). Secondary antibodies conjugated to Alexa (−488, −555 and −647; Molecular Probes) were used at a 1:300 dilution in a 2 h incubation at room temperature. Isolectin B4 (1:200; Vector Labs) and Cy3 and FITC-conjugated anti-αSMA mouse mAb (1:300; Sigma Aldrich) were used under the same conditions as the secondary antibodies. Images were acquired with an LD C-Apochromat ×40, 1.1 numerical aperture water-immersion objective attached to an Axiovert 200M inverted microscope (Zeiss), equipped with a CSU10 spinning disc confocal scan head (Yokogawa Electric) and an Evolve EMCCD camera (Photometrics). A DF5000B Leica fluorescent microscope was used to image 10-µm thick heart sections. Image processing and analysis was performed with Fiji or ImageJ software FIJI 1.49a (64-bit).

Statistical analysis. Data normality was evaluated by the Shapiro–Wilk test. Mann–Whitney U-test was used accordingly to determine statistically significant differences between groups, with a statistical significance threshold of $P \leq 0.05$. For data assumed to be normally distributed, either a two-tailed Student's t-test or a one-way analysis of variance (ANOVA) with Bonferroni post hoc correction was used, with a statistical significance threshold of $P \leq 0.01$.

Data availability. The authors declare that all data supporting the findings of this study are available within the paper and its Supplementary Information.

References
1. *Underlying Cause of Death 1999–2013 CDC WONDER Online Database* (Centers for Disease Control and Prevention, National Center for Health Statistics, accessed 3 February 2015); https://wonder.cdc.gov/ucd-icd10.html
2. *Deaths, Percent of Total Deaths, and Death Rates for the 15 Leading Causes of Death: United States and Each State, 1999–2014* (Centers for Disease Control and Prevention, National Center for Health Statistics, 2015).

3. Mozaffarian, D. *et al.* Heart disease and stroke statistics—2015 update: a report from the American Heart Association. *Circulation* **131**, 29–322 (2015).

4. Fryar, C. D., Chen, T. C. & Li, X. Prevalence of uncontrolled risk factors for cardiovascular disease: United States, 1999–2010. *NCHS Data Brief* **103**, 1–8 (2012).

5. Fowkes, F. G. *et al.* Comparison of global estimates of prevalence and risk factors for peripheral artery disease in 2000 and 2010: a systematic review and analysis. *Lancet* **382**, 1329–1340 (2013).

6. Hall, M. J., DeFrances, C. J., Williams, S. N., Golosinskiy, A. & Schwartzman, A. National Hospital Discharge Survey: 2007 summary. *Natl Health Stat. Rep.* **29**, 1–20 (2010).

7. Conte, M. S. Bypass versus angioplasty in severe ischaemia of the leg (BASIL) and the (hoped for) dawn of evidence-based treatment for advanced limb ischaemia. *J. Vasc. Surg.* **51**, 69S–75S (2010).

8. Salacinski, H. J. *et al.* The mechanical behavior of vascular grafts: a review. *J. Biomater. Appl.* **15**, 241–278 (2001).

9. Slovut, D. P. & Lipsitz, E. C. Surgical technique and peripheral artery disease. *Circulation* **126**, 1127–1138 (2012).

10. Kakkar, A. M. & Abbott, J. D. Percutaneous versus surgical management of lower extremity peripheral artery disease. *Curr. Atheroscler. Rep.* **17**, 479 (2015).

11. Kappetein, A. P., Van Mieghem, N. M. & Head, S. J. Revascularization options: coronary artery bypass surgery and percutaneous coronary intervention. *Cardiol. Clin.* **32**, 457–461 (2014).

12. L'Heureux, N. *et al.* Human tissue-engineered blood vessels for adult arterial revascularization. *Nat. Med.* **12**, 361–365 (2006).

13. Dahl, S. L. *et al.* Readily available tissue-engineered vascular grafts. *Sci. Transl. Med.* **3**, 68ra9 (2011).

14. Quint, C. *et al.* Decellularized tissue-engineered blood vessel as an arterial conduit. *Proc. Natl Acad. Sci. USA* **108**, 9214–9219 (2011).

15. Henry, T. D. *et al.* The VIVA trial: vascular endothelial growth factor in ischaemia for vascular angiogenesis. *Circulation* **107**, 1359–1365 (2003).

16. Simons, M. *et al.* Pharmacological treatment of coronary artery disease with recombinant fibroblast growth factor-2: double-blind, randomized, controlled clinical trial. *Circulation* **105**, 788–793 (2002).

17. Giacca, M. & Zacchigna, S. VEGF gene therapy: therapeutic angiogenesis in the clinic and beyond. *Gene Ther.* **19**, 622–629 (2012).

18. Ferrara, N. The role of vascular endothelial growth factor in pathological angiogenesis. *Breast Cancer Res. Treat.* **36**, 127–137 (1995).

19. Peters, M. C., Polverini, P. J. & Mooney, D. J. Engineering vascular networks in porous polymer matrices. *J. Biomed. Mater. Res.* **60**, 668–678 (2002).

20. Ehrbar, M. *et al.* Cell-demanded liberation of VEGF121 from fibrin implants induces local and controlled blood vessel growth. *Circ. Res.* **94**, 1124–1132 (2004).

21. Phelps, E. A., Landázuri, N., Thulé, P. M., Taylor, W. R. & García, A. J. Bioartificial matrices for therapeutic vascularization. *Proc. Natl Acad. Sci. USA* **107**, 3323–3328 (2010).

22. Sadr, N. *et al.* SAM-based cell transfer to photopatterned hydrogels for microengineering vascular-like structures. *Biomaterials* **32**, 7479–7490 (2011).

23. Gupta, R., Tongers, J. & Losordo, D. W. Human studies of angiogenic gene therapy. *Circ. Res.* **105**, 724–736 (2009).

24. Koike, N. *et al.* Tissue engineering: creation of long-lasting blood vessels. *Nature* **428**, 138–139 (2004).

25. Au, P., Tam, J., Fukumura, D. & Jain, R. K. Bone marrow-derived mesenchymal stem cells facilitate engineering of long-lasting functional vasculature. *Blood* **111**, 4551–4558 (2008).

26. Kusuma, S. *et al.* Self-organized vascular networks from human pluripotent stem cells in a synthetic matrix. *Proc. Natl Acad. Sci. USA* **110**, 12601–12606 (2013).

27. Levenberg, S. *et al.* Engineering vascularized skeletal muscle tissue. *Nat. Biotechnol.* **23**, 879–884 (2005).

28. Baranski, J. D. *et al.* Geometric control of vascular networks to enhance engineered tissue integration and function. *Proc. Natl Acad. Sci. USA* **110**, 7586–7591 (2013).

29. Miller, J. S. *et al.* Rapid casting of patterned vascular networks for perfusable engineered three-dimensional tissues. *Nat. Mater.* **11**, 768–774 (2012).

30. Hiesinger, W. *et al.* Computational protein design to reengineer stromal cell-derived factor-1α generates an effective and translatable angiogenic polypeptide analog. *Circulation* **124**, S18–S26 (2011).

31. MacArthur, J. W. *et al.* Mathematically engineered stromal cell-derived factor-1α stem cell cytokine analog enhances mechanical properties of infarcted myocardium. *J. Thorac. Cardiov. Sur.* **145**, 278–284 (2013).

32. MacArthur, J. W. *et al.* Sustained release of engineered stromal cell-derived factor 1-α from injectable hydrogels effectively recruits endothelial progenitor cells and preserves ventricular function after myocardial infarction. *Circulation* **128**, S79–S86 (2013).

33. Shudo, Y. *et al.* A tissue-engineered chondrocyte cell sheet induces extracellular matrix modification to enhance ventricular biomechanics and attenuate myocardial stiffness in ischaemic cardiomyopathy. *Tissue Eng. Part A* **19–20**, 2515–2525 (2015).

34. Rodell, C. B. *et al.* Shear-thinning supramolecular hydrogels with secondary autonomous covalent crosslinking to modulate viscoelastic properties *in vivo*. *Adv. Funct. Mater.* **25**, 636–644 (2015).

35. Murray, C. D. The physiological principle of minimum work: I. The vascular system and the cost of blood volume. *Proc. Natl Acad. Sci. USA* **12**, 207–214 (1926).

36. Kassab, G. S. Scaling laws of vascular trees: of form and function. *Am. J. Physiol. Heart C* **290**, H894–H903 (2006).

37. Kang, H.-W., Atala, A. & Yoo, J. J. in *Essentials of 3D Biofabrication and Translation* (eds Atala, A. & Yoo, J. J.) Ch. 10 (Elsevier, 2015).

38. Visconti, R. P. *et al.* Towards organ printing: engineering an intra-organ branched vascular tree. *Expert Opin. Biol. Ther.* **10**, 409–420 (2010).

39. Sydney Gladman, A., Matsumoto, E. A., Nuzzo, R. G., Mahadevan, L. & Lewis, J. A. Biomimetic 4D printing. *Nat. Mater.* **15**, 413–418 (2016).

40. Moroni, F. & Mirabella, T. Decellularized matrices for cardiovascular tissue engineering. *Am. J. Stem Cells* **13**, 1–20 (2014).

41. Sooppan, R. *et al.* *In vivo* anastomosis and perfusion of a three-dimensionally-printed construct containing microchannel networks. *Tissue Eng. Part C* **22**, 1–7 (2016).

42. Jaipersad, A. S., Lip, G. Y., Silverman, S. & Shantsila, E. The role of monocytes in angiogenesis and atherosclerosis. *J. Am. Coll. Cardiol.* **63**, 1–11 (2014).

43. Waters, R. E., Terjung, R. L., Peters, K. G. & Annex, B. H. Preclinical models of human peripheral arterial occlusive disease: implications for investigation of therapeutic agents. *J. Appl. Physiol.* **97**, 773–780 (2004).

44. Hall, M. J. *et al.* National Hospital Discharge Survey: 2007 summary. *Natl Health Stat. Report* **24**, 1–20 (2010).

45. Norgren, L. *et al.* Inter-society consensus for the management of peripheral arterial disease (TASC II). *J. Vasc. Surg.* **45**, S5–67 (2007).

46. Belch, J. J. *et al.* Critical issues in peripheral arterial disease detection and management: a call to action. *Arch. Intern. Med.* **163**, 884–892 (2003).

47. Al Mahameed, A. Peripheral arterial disease. *Cleveland Clinic Center for Continuing Education* http://www.clevelandclinicmeded.com/medicalpubs/diseasemanagement/cardiology/peripheral-arterial-disease/ (2009).

48. Hoefer, I. E. *et al.* Arteriogenesis proceeds via ICAM-1/Mac-1-mediated mechanisms. *Circ. Res.* **94**, 1179–1185 (2004).

49. Mirabella, T., Cilli, M., Carlone, S., Cancedda, R. & Gentili, C. Amniotic liquid derived stem cells as reservoir of secreted angiogenic factors capable of stimulating neo-arteriogenesis in an ischaemic model. *Biomaterials* **32**, 3689–3699 (2011).

50. Mirabella, T. *et al.* Proangiogenic soluble factors from amniotic fluid stem cells mediate the recruitment of endothelial progenitors in a model of ischaemic fasciocutaneous flap. *Stem Cells Dev.* **21**, 2179–2188 (2012).

51. National Research Council *Guide for the Care and Use of Laboratory Animals* 8th edn (National Academies, 2011).

Author contributions

T.M., J.W.M., D.C., C.K.O., Y.J.W., M.T.Y. and C.S.C. conceived, developed and mentored the project. T.M., J.W.M., D.C. and M.T.Y. performed the experiments. T.M. and J.W.M. analysed the data. T.M. and C.S.C. wrote the manuscript.

Additional information

Supplementary information is available for this paper.

Reprints and permissions information is available at www.nature.com/reprints.

Correspondence and requests for materials should be addressed to C.S.C.

How to cite this article: Mirabella, T. *et al.* 3D-printed vascular networks direct therapeutic angiogenesis in ischaemia. *Nat. Biomed. Eng.* **1**, 0083 (2017).

Publisher's note: Springer Nature remains neutral with regard to jurisdictional claims in published maps and institutional affiliations.

Competing interests

C.S.C. is a cofounder of, and owns equity in, Innolign Biomedical, a company that is developing tissue-engineered products.